Cherns, D., Griffiths, I., Jones, L., Bishop, D., Lloyd, M., & McCandless, B. (2018). Direct Observation of High Densities of Antisite Defects in Ag2ZnSnSe4. *ACS Applied Energy Materials*, *1*(11), 6260-6267. https://doi.org/10.1021/acsaem.8b01274

Article

Direct Observation of High Densities of Antisite Defects in Ag2ZnSnSe4

David Cherns, Ian Griffiths, Lewys Jones, Douglas Bishop, Michael Lloyd, and Brian E. McCandless

ACS Appl. Energy Mater., **Just Accepted Manuscript** • DOI: 10.1021/acsaem.8b01274 • Publication Date (Web): 19 Oct 2018

Direct Observation of High Densities of Antisite Defects in $Ag_2ZnSnSe_4$

David Cherns[1*], Ian J. Griffiths[2], Lewys Jones[3], Douglas M. Bishop[4], Michael A. Lloyd[5] and Brian E. McCandless[5]

1. School of Physics, University of Bristol, Tyndall Avenue, Bristol BS8 1TL, UK
2. Department of Materials, University of Oxford, Parks Road, Oxford OX1 3PH, UK
3. School of Physics & CRANN, Trinity College Dublin, the University of Dublin, Dublin 2, D02 PN40, Ireland
4. IBM T. J. Watson Research Center, Yorktown Heights, New York 10598, USA
5. Institute of Energy Conversion, University of Delaware, Newark, Delaware, 19716, USA

*Corresponding author email: d.cherns@bristol.ac.uk

Keywords: thin film solar cells; $Ag_2ZnSnSe_4$; $Cu_2ZnSnSe_4$; antisite defects; scanning transmission electron microscopy; atomic resolution energy dispersive X-ray analysis

Abstract

The limited efficiency of $Cu_2ZnSn(SSe)_4$ (CZTSSe) solar cells has been widely attributed to band tailing due to high densities of Cu_{Zn} and Zn_{Cu} antisite defects. It has been proposed that partial replacement of Cu by Ag should reduce the antisite defect density, leading to reduced band tailing and increased cell efficiencies. This paper examines antisite defects in $Ag_2ZnSnSe_4$ (AZTSe) crystals grown at high temperatures from a stoichiometric mixture of elements by scanning transmission electron microscopy (STEM), X-ray diffraction (XRD) and photoluminescence (PL). The elemental distribution was examined directly by atomic resolution STEM energy-dispersive X-ray (EDX) mapping and simultaneous annular dark field (ADF) imaging. EDX mapping suggested complete intermixing of Ag and Zn on the Wyckoff 2c and 2d sites in the AZTSe kesterite unit cell, and around 14% substitution of Zn for Ag on the 2a site, while ADF images showed evidence for local nanometer-sized regions within the disordered matrix with partial ordering of Zn and Ag on the 2c and 2d sites. These observations show that the AZTSe had a high density of Ag_{Zn} and Zn_{Ag} antisite defects, in contrast with room temperature photoluminescence showing relatively narrow emission lines close to the band edge and thus minimal band tailing. The interpretation of these results, and their wider significance for understanding the role of antisite defects in CZTSSe and Ag-substituted CZTSSe cells, are discussed.

1. Introduction:

Thin film photovoltaic (PV) solar cells based on CdTe and $CuInGaSe_2$ (CIGS) account for nearly 5% of the solar cell market. However, there is increasing concern that these absorber materials

contain elements which are either in short supply (particularly In, Te) or toxic (Cd). There is interest in developing replacement materials with similar structure and electronic properties, but composed of less toxic and more earth-abundant elements. One such material is $Cu_2ZnSn(SSe)_4$ (CZTSSe), which has a band-gap in the range 1.0-1.5 eV. However, whereas CdTe and CIGS cells with similar band-gaps have efficiencies up to about 22%, the best CZTSSe cells are still below 13% efficiency.[1] This has been widely ascribed to antisite defects, particularly Cu_{Zn} and Zn_{Cu} which are known to be present at high densities in the equilibrium kesterite structure from neutron and synchrotron X-ray diffraction, Raman and scanning transmission electron microscopy (STEM) studies.[2-6] These defects, either in the form of Cu-Zn antisite pairs, or as single antisite defects which carry a net charge, have been considered to account for the "band tailing" apparent in optical data from CZTSSe.[7,8] This, in turn, is theorized to account for the low open circuit voltage (V_{OC}), typically around 60% of the theoretical maximum, which is a principal reason for the limited cell efficiency.[9] Cu-Zn antisite defects should form easily in CZTSSe as the estimated energy for exchange of an isolated pair of Cu-Zn ions is around 0.2 eV, partly due to the Cu^+ having a covalent radius around 5% larger than Zn^{2+}, leading to a relatively low strain energy contribution.[10] Replacement of Cu^+ by Ag^+, which has a covalent radius around 17% greater than Zn^{2+}, has been estimated to increase this ion exchange energy by a factor of about 4, such that antisite defect densities should be reduced by more than an order of magnitude.[11] Experimentally, photoluminescence (PL) studies of Ag-substituted CZTSSe show a progressive reduction in band tailing as the Ag content increases, and for low levels of Ag substitution, modest increases in cell efficiencies have been noted.[12] The implication, as yet

unverified, is that Ag-substitution has reduced densities of antisite defects compared with CZTSSe, and that this is a key factor in improving cell efficiencies.

In this paper we use STEM to directly examine Ag-Zn ordering in $Ag_2SnZnSe_4$ (AZTSe) for the first time. In previous STEM work, we have used atomic resolution high angle ADF (HAADF) imaging in the [010] orientation to examine cation ordering in CZTS.[13] For a completely ordered kesterite structure viewed along [010] (Figure 1), the individual end-on atom columns in CZTS are composed of a single element, Sn, Cu, Zn or S. Since HAADF images show contrast which increases with the atomic number Z, [010] atomic resolution images distinguish the Sn (Z=50) columns as the sites of highest intensity from the Cu (Z=29), Zn (Z=30) or S (Z=16) columns. The images revealed high densities of antisite domain boundaries through relative shifts of the Sn columns across edge-on boundaries (e.g. see figures 3,4 in [13]). Although the Cu and Zn columns are essentially indistinguishable in HAADF owing to their close atomic numbers, Mendis et al.[5] used atomic resolution electron energy loss spectroscopy (EELS) in STEM to map the Cu and Zn distribution in [010]-oriented CZTS. They found some evidence of Cu-Zn intermixing on the Wyckoff 2c and 2d sites (defined in Figure 1), as well as Cu and Zn clustering on a 1-5nm scale. Aguiar et al.[6] used atomic resolution EELS mapping in a [112] orientation to show further evidence for clustering of Cu and Zn in CZTS, albeit on a slightly broader (20nm) scale.

Here, we combine HAADF imaging with atomic resolution elemental mapping by energy dispersive X-ray microanalysis (EDX) in the [010] orientation. The results, which enable us to map the distribution of all four elements, show that there are regions of near-complete intermixing of Ag and Zn on the Wyckoff 2c and 2d sites, along with less but significant

intermixing of Ag and Zn on the Wyckoff 2a sites. Despite this evidence for high densities of Ag-Zn antisite defects, photoluminescence measurements show a relatively narrow emission close to the expected band edge. The interpretation of these results, and the wider implications for understanding the properties and the role of antisite defects in CZTSSe and Ag-substituted cells, are discussed.

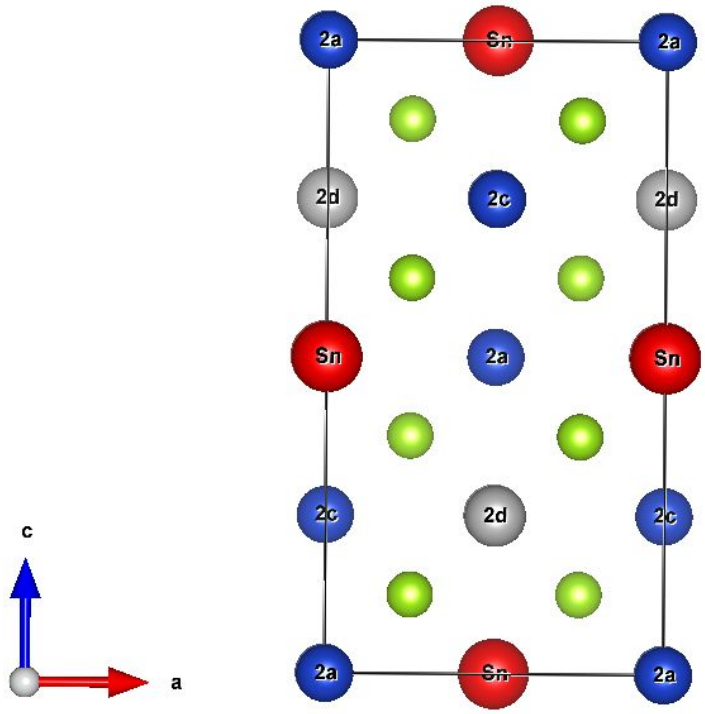

Figure 1: The unit cell for kesterite CZTSSe or AZTSSe viewed down the b-axis [010]. Red: Sn columns; green (unlabelled): S or Se columns. The remaining columns are Wyckoff sites 2a (Cu/Ag, blue), 2c (Cu/Ag, blue) and 2d (Zn, grey)

2. Experimental methods:

$Ag_2SnZnSe_4$ was grown at high temperature in an evacuated sealed ampoule from a stoichiometric mixture of the pure elements.[14] The elemental mixture was sealed in a quartz

ampoule at 10^{-6} torr and annealed for 20 days at 480°C. The material was then extracted and ground to a powder to homogenise it, re-sealed under vacuum in a second ampoule and annealed for a further 26 days at 510°C. The resulting material was then divided into two samples, one of which was quenched into ice-water, and the other slow-cooled to room temperature, at 3°C/hr, to maximise ordering.

Both samples were powders with occasional crystals up to 1 mm or more across, along with micron-sized crystals. The general morphology and composition were studied in an Amray 1810T Digital Scanning Electron Microscope (SEM) with Energy Dispersive Spectroscopy. Bulk structural analysis was performed via X-ray diffraction (XRD) using a Philips/Norelco scanning wide angle X-ray diffractometer with Bragg-Brentano geometry. XRD specimens were gently pulverized in an agate crucible with 125 mesh in accordance with ASTM standards. Lattice parameters were determined using JADE XRD analysis software (Materials Data, Inc. (MDI) JADE 2010) for unit cell Rietveld refinements.

For STEM, samples were ground into a fine powder and dispersed in pure ethanol onto holey carbon films. The films were then heated to 90°C under vacuum for 12hr to remove hydrocarbons and examined in a JEOL ARM200CF (S)TEM operating with a cold field emission source and aberration correction on the probe, giving a probe size less than 0.1nm. HAADF imaging and simultaneous EDX microanalysis using a single Centurio 100mm^2 detector were carried out in scanning (STEM) mode. HAADF images shown in this paper have inner and outer cut-off angles of 73 mrad and 236 mrad respectively.

Photoluminescence was carried out on the as-grown powders at room temperature using a 532 nm pulsed laser operating at 15 kHz with a photomultiplier tube and InGaAs detector. A neutral density filter wheel was used to change incident laser intensity.

3. Results and discussion:

3.1 SEM and XRD

Figure 2 shows SEM and XRD results from the slow-cooled sample. Figure 2a illustrates the as-grown material and a magnified view of a group of individual AZTSe grains, with near stoichiometric composition as confirmed by EDX spot measurements. In Figure 2b, the experimental XRD pattern is compared with a simulation in red for the fully ordered $Ag_2SnZnSe_4$ kesterite structure (Figure 1). The main peaks in the XRD are consistent with the kesterite phase, with lattice constants of a = 6.03 ± 0.01 Å and a c/a value of 1.88 ± 0.01 similar to previous reports.[15] Evidence of secondary phases, including $SnSe_2$ and ZnSe can also be detected in the powder due to the large XRD sampling volume. The major $Ag_2SnZnSe_4$ peaks, such as hkl = 112, 220, 312 etc, represent the underlying near-cubic face-centred lattice obtained if the ordering of the cations, Sn, Ag and Zn, is ignored (i.e. corresponding to a unit cell half that in Figure 1, with dimensions a, a, c/2). Minor $Ag_2SnZnSe_4$ peaks such as 002, 101 and 110, with intensities typically a few percent of the major peak intensities, are also present due to cation ordering. It is worth noting that the 101 reflection is sensitive to Ag-Zn ordering on the Wyckoff 2c and 2d sites, and is kinematically forbidden in a model where Ag and Zn are completely intermixed on these sites. The 101 reflection was present for the quenched as well as the slow-cooled sample but with an intensity about 30% lower.

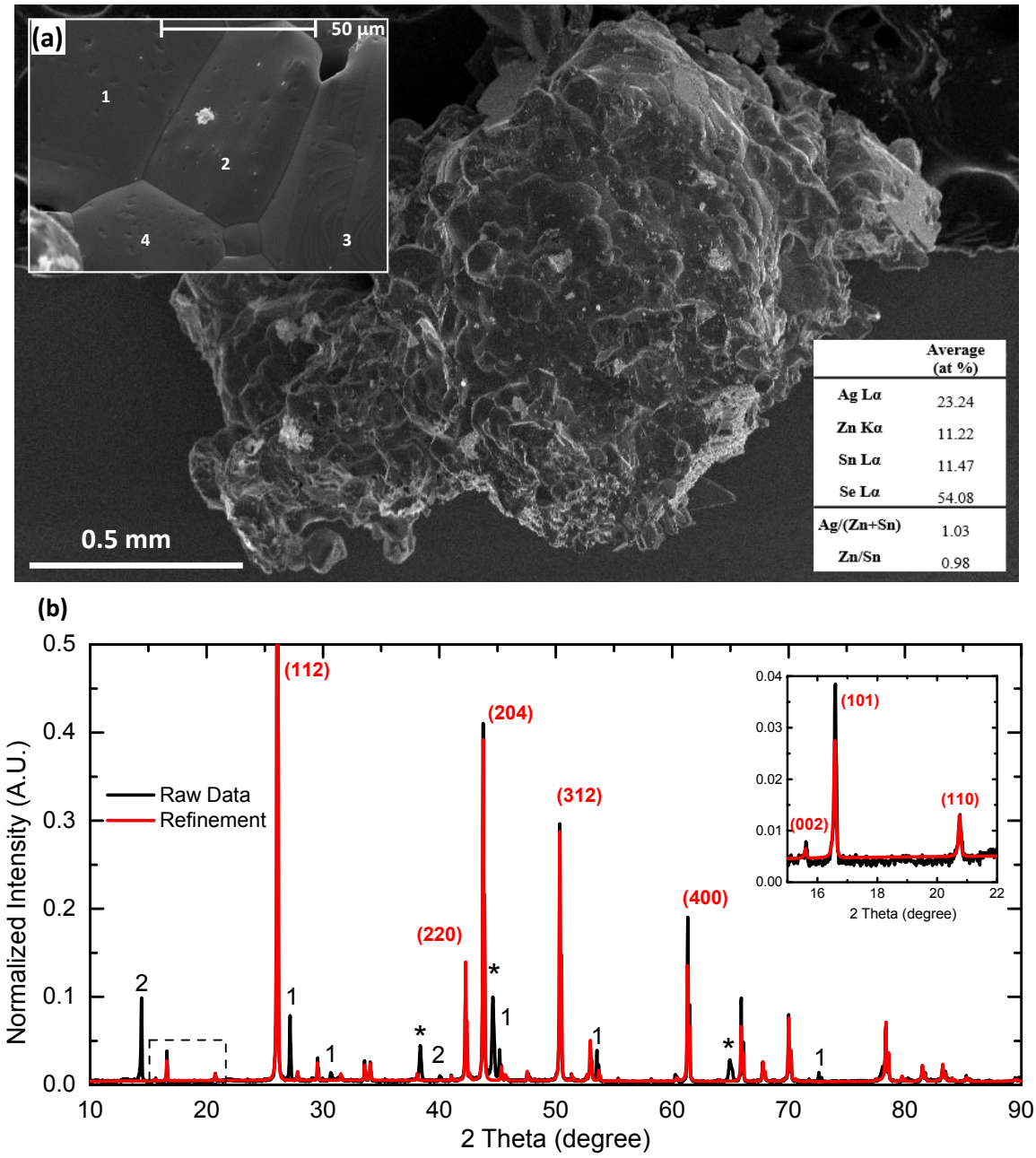

Figure 2: (a) SEM micrograph of synthesized AZTSe powder. Insert: Magnified AZTSe grains with numbered regions of interest. Table: Average EDX composition of regions 1-4, (b) XRD pattern for the slow-cooled sample (black) and fit for ordered AZTSe model (red).

3.2 STEM

While XRD is relatively insensitive to cation ordering in this system and provides only a view of aggregate structure across thousands of crystals/ grains, STEM allows us to select single crystal particles of $Ag_2SnZnSe_4$ and tilt them to “structure sensitive” orientations such as [010] where cation ordering can be examined in more detail.

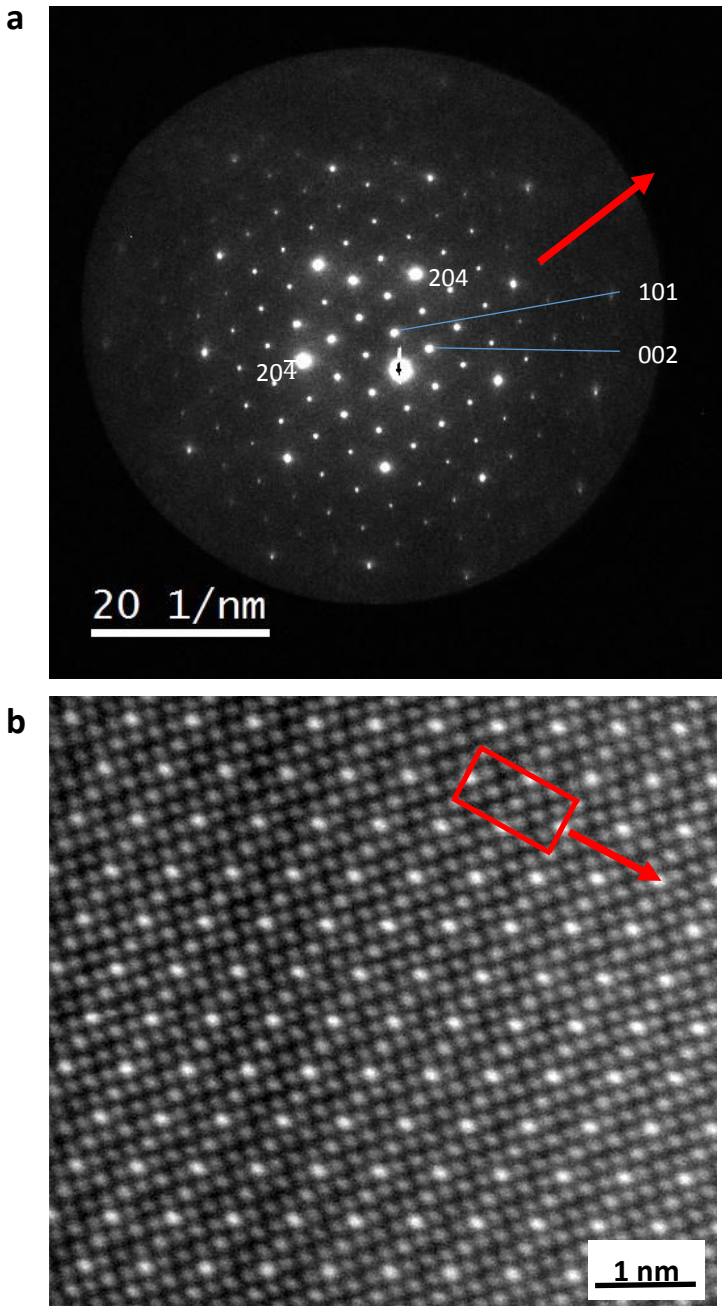

Figure 3: (a) selected area diffraction pattern and (b) HAADF image of AZTSe (unit cell outlined) viewed down the b-axis. The c-axis is arrowed in (a) and (b). As for CZTS in Figure 1(b), the brightest spots in the HAADF image, which form a near-hexagonal array

The STEM samples contained well separated micrometer-sized particles. Selection and tilting of particles to the [010] orientation was carried out in direct imaging (TEM) mode, with a near-parallel incident beam. Figure 3a shows a typical electron diffraction pattern taken from

one such particle in the [010] orientation. This illustrates that, in contrast to XRD, the intensities of the cation ordering reflections 002, 101 etc are relatively increased, although not directly interpretable owing to dynamical scattering, compared with the major reflections 204 and 20-4 (Figure 2b). The microscope was then changed to scanning (STEM) mode, and HAADF and EDX mapping were carried out. Figure 3b shows a HAADF image of the slow-cooled AZTSe taken with [010] parallel to the beam. The atomic numbers for Sn (Z=50) and Ag (Z=47) are relatively close, and therefore the intensities on Sn and Ag (Wyckoff 2a and 2c) sites should be similar, with much lower intensity for Zn (Z=30, Wyckoff 2d) sites. However, the HAADF image shows a near-hexagonal array of bright spots, which we identify later as the Sn columns, and lower, and relatively similar intensities for other cation columns (Wyckoff 2a, 2c and 2d sites) corresponding to mixtures of Ag and Zn.

In order to unambiguously identify the elemental distribution, we have correlated HAADF images with simultaneous EDX mapping, using methods of data superposition described by Jones et al.[16,17] The final results are shown in Figure 4 and more detail is shown in the Supplementary data. In summary, HAADF images and EDX spectra were recorded by scanning a 0.1nm probe, with 17pA current, over an 11nm x 11nm area of single crystal. Owing to low X-ray count rates, repeated scans were carried out for the same or a closely adjacent area to minimise radiation damage effects, and the HAADF (along with the EDX) maps aligned by non-rigid registration, correcting for the effects of specimen drift and scan distortions.[17] In this procedure, the bright spots in the HAADF images of AZTSe (Sn columns) act as a reliable reference lattice to bring successive frames into coincidence. To obtain the results shown in

Figure 4, a tile was then defined in the extended scan, and

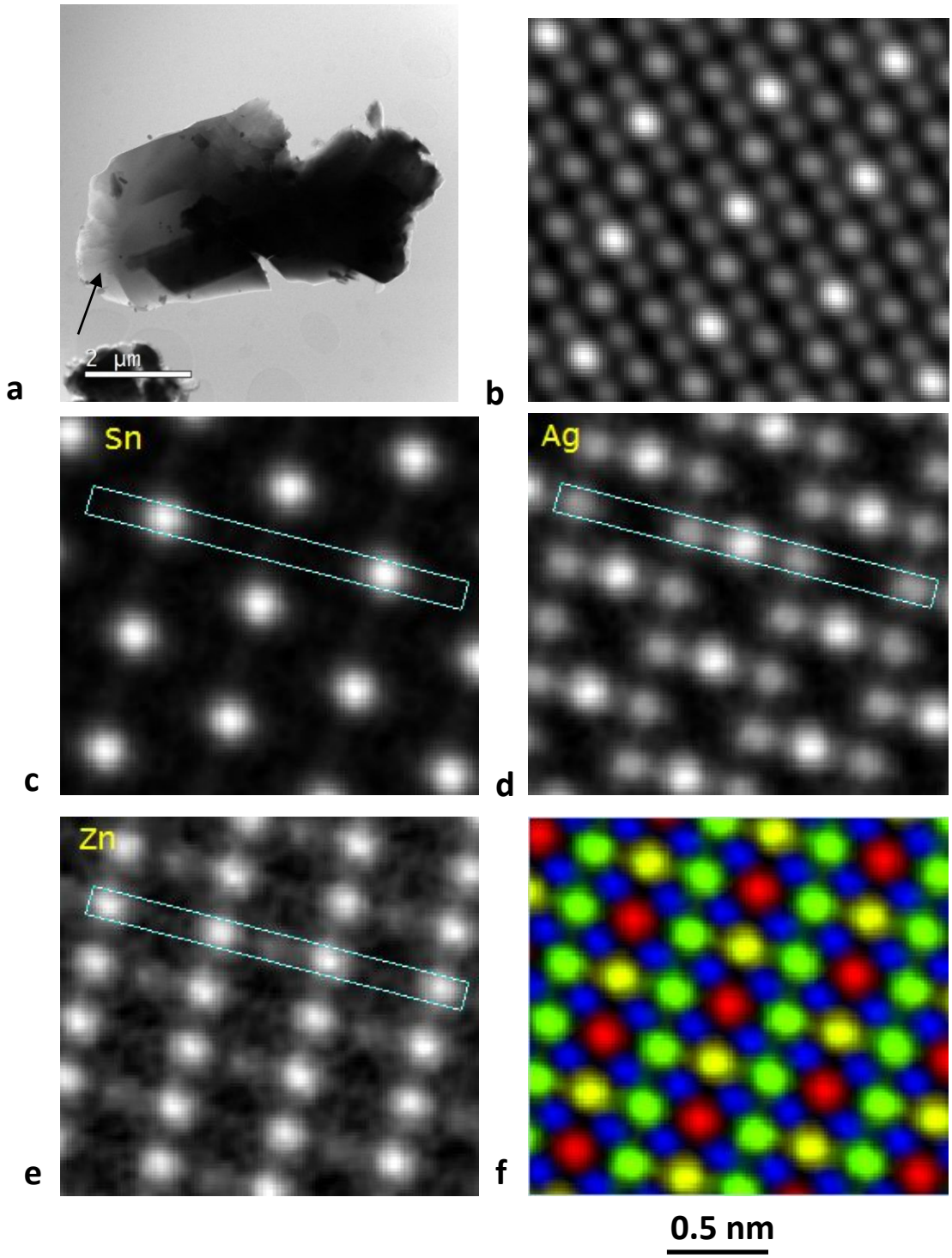

Figure 4: Simultaneous HAADF and EDX mapping, (a) area selected (arrowed), (b) HAADF, (c-e) EDX maps for Sn L, Ag L and Zn L X-rays following data superposition, (f) colour montage: red - Sn; yellow - Ag in 2a site; green - Zn and Ag in 2c/2d sites; blue - Se K

template matching was used to identify 111 other unique tiles. Summing over these further improves the signal to noise ratio, giving an effective electron dose corresponding to the HAADF and EDX maps in Figure 3 of 8.9×10^{11} $e^{-}nm^{-2}$.

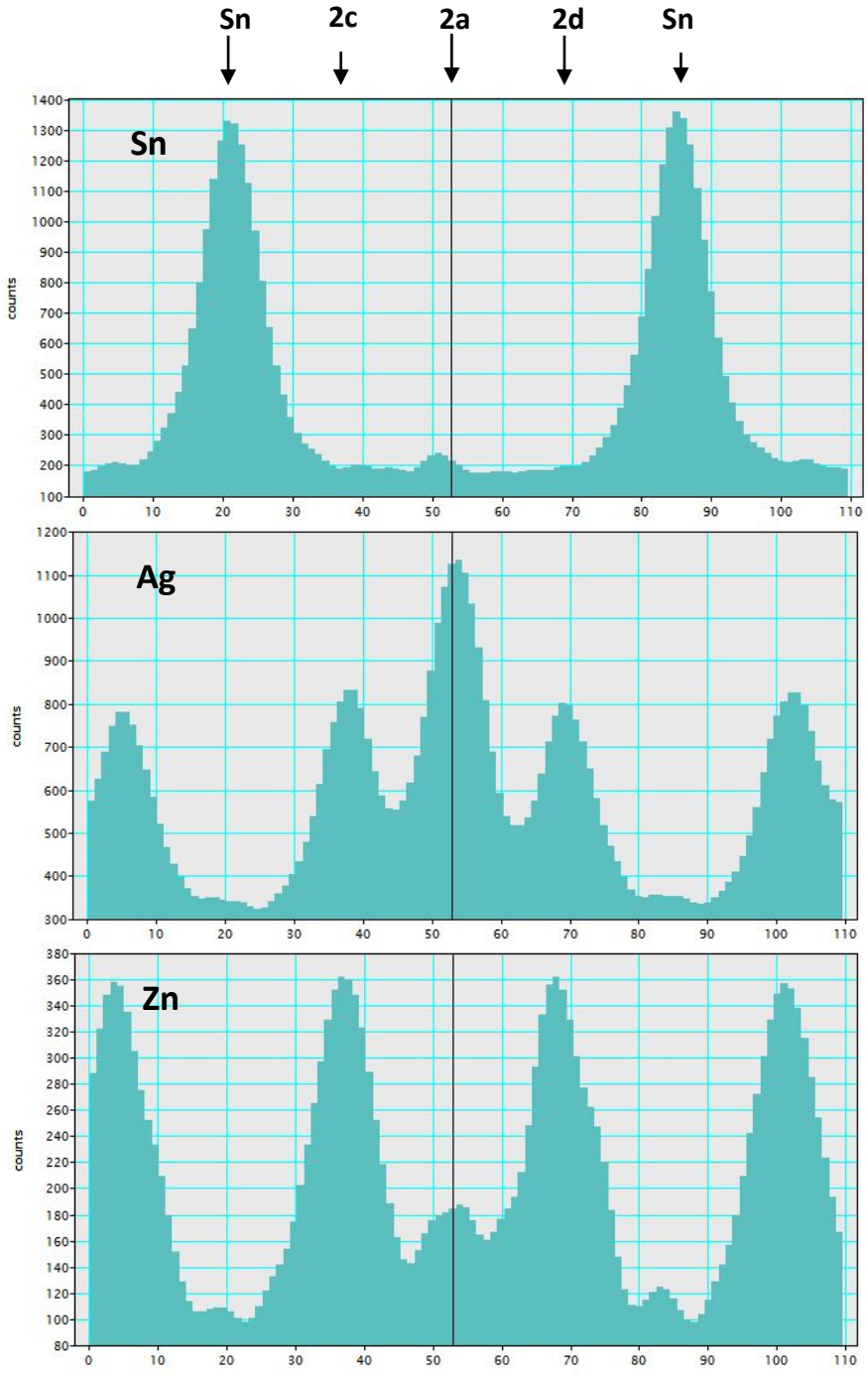

Figure 5: Intensity linescans parallel to the c-axis for the areas outlined in Figure 4. The linescans pass through the 2a, 2c, 2d and Sn sites as indicated

The results in Figure 4 show the average distributions of Sn, Ag and Zn from an area some tens of nanometers across and estimated to be 20-30nm thick from a t/λ fit to EELS

spectra.[18] Linescans in the [001] direction across the EDX maps in Figure 4 are shown in Figure 5, and compare the distributions of Sn, Ag and Zn across all three cation sites. The higher concentration of Ag on the 2a site compared with the 2c and 2d sites confirms that the basic structure is kesterite rather than stannite, which is a slightly higher energy structure with Zn on the 2a site.[19] We note that the distinction between sites 2c and 2d is arbitrary, as, within the experimental error, neither the HAADF nor the EDX maps show a clear difference between these sites. Despite the superimposition of many images, Fourier analysis gave the real-space resolution in the HAADF images as 0.094nm, and the resolution in the EDX maps in the range 0.16-0.20 nm. In the thin crystal limit, EDX spatial resolution is expected to be not much larger than the probe size as X-ray generation depends on a localised interaction of the incident electron beam with tightly bound inner electron shells. As the focussed probe is scanned across a given atom column, electron dechannelling (beam spreading) due to thermal diffuse scattering should contribute to some broadening of the X-ray peaks and also cause some X-rays to be generated on neighbouring atom columns. Calculations[20] suggest that is likely to be a small contribution at the film thicknesses here (20-30nm), but this will depend on the Debye-Waller factors for AZTSe, which are not known at present, and might include a significant static component as Ag and Zn intermixing should cause ions to be displaced from lattice sites owing to the disparity in the Ag and Zn ionic radii.[21] Taking the Sn map and line profiles in Figures 5, there is a good correspondence between the bright spots in the HAADF image peaks and the main peaks in the Sn L map, confirming our earlier assumption that the bright spots in HAADF maps represent Sn columns. There is also a small Sn peak on the 2a column (less than 4% of the main peaks), and similar small Ag and Zn peaks on the Sn sites. These subsidiary peaks will

include the dechannelling contribution, confirming that the dechannelling contribution is small. However, whether these subsidiary peaks are wholly due to dechannelling or include a proportion of elemental intermixing remains uncertain.

The EDX maps confirm that Ag and Zn are both present in the 2c and 2d sites in about equal amounts within random error limits (i.e. $N \mp \sqrt{N}$ where *N* is the number of X-ray counts) and that there is also a significant Zn peak in the 2a site. Table 1 shows the atomic fractions of Ag and Zn in all three sites, calculated separately from the Ag and Zn profiles. In calculating these fractions, it has been assumed that in total, over all three sites, the Ag and Zn were present in stoichiometric amounts (i.e. two Ag and one Zn atom per unit cell) and that the subsidiary Ag and Zn peaks on the Sn sites measure the dechannelling contribution from neighbouring 2a, 2c and 2d sites only, i.e. no Ag or Zn in the Sn columns. The dechannelling contribution to each of the 2a, 2c and 2d peaks will depend on the location of neighbouring columns with the same element and the extent of dechannelling. As the latter is not known, we have assumed, for simplicity, that the dechannelling peak on the Sn site represents a fixed contribution to be subtracted from all peaks.

Table 1: Zn and Ag atomic fractions estimated from the respective Zn and Ag maps

	2a site	2c site	2d site
Zn fraction from Zn map	0.14 ± 0.03	0.43 ± 0.02	0.43 ± 0.02
Ag fraction from Ag map	0.89 ± 0.02	0.57 ± 0.02	0.55 ± 0.02

In interpreting the data in Table 1, it is necessary to consider whether the Ag and Zn are randomly distributed in the 2a, 2c and 2d columns or whether there is local ordering. To investigate this, we have examined individual HAADF images. In general, the HAADF intensity is known to be relatively simply related to Z, varying as approximately $Z^{1.7}$ over a wide range of imaging conditions.[22,23] However, static atomic displacements from idealized kesterite coordinates can affect quantitative analysis of column compositions, and may be expected in our case.[21] Nevertheless, HAADF images taken from different areas of both the slow-cooled and quenched samples showed clear evidence for localised regions with partial ordering, as indicated by an asymmetry in the intensity between 2c and 2d sites. This is evident from Figure 6, which illustrates a HAADF image from the quenched sample, along with a linescan taken along the [100] direction through the 2c and 2d sites. This shows two localised regions A and B with evidence of ordering on the alternating 2c/2d sites, i.e. every second peak is more intense, indicating relatively more Ag. Between A and B there is a relative reversal in the ordering.

In order to reconcile the apparently different results in Figures 5 and 6, one possibility is that the AZTSe has neighbouring regions of ordered kesterite with a relative rotation of 180° about [010] which bring the Sn columns back into coincidence. Structurally this corresponds to a twin relationship between domains. For a single end-on column containing both domains, this would superimpose the 2c and 2d sites, giving apparently equal Zn and Ag occupancy if the domains were present in equal amounts. However, this model would not account for the presence of Zn in the 2a columns since these columns would be unaffected by the transformation. In addition, if twins were present, we should also expect them to be limited laterally along the [100] direction, which is crystallographically equivalent to [010]. This would

lead to local reversals in the 2c/2d asymmetry of the type seen in Figure 6. In this case, the transition between neighbouring domains takes place over 1-2nm. Whether this reflects the width of the boundary region, or the boundary is atomically sharp but inclined is, however, unclear. Indeed, we found no clear evidence in the HAADF images from either the quenched and slow-cooled samples for abrupt twin boundaries. This suggests that the transition region between ordered domains has a finite width, but further studies are needed to confirm this

point.

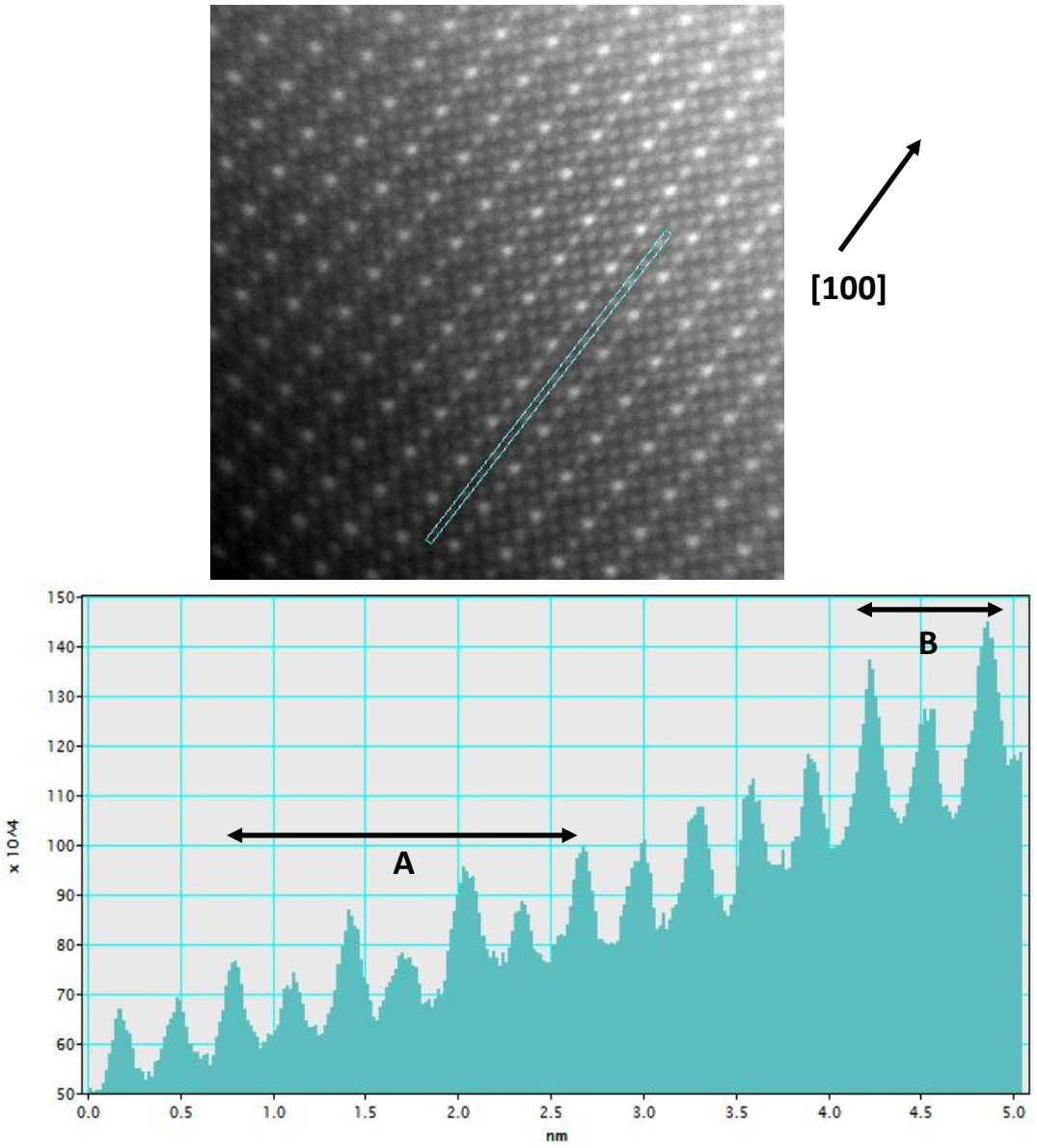

Figure 6: HAADF image from the quenched sample, and intensity linescan in the [100] direction along the 2c-2d row (Figure 1) for the region indicated. A and B show regions of local asymmetry in intensity between the 2c and 2d sites

The HAADF results therefore suggest a model where there is local (nanoscale) Zn-Ag ordering on the 2c and 2d sites and a twin relationship between ordered regions. This is therefore consistent with the observation of reflections such as 101 in XRD which are

kinematically forbidden for perfect Ag-Zn disorder on the 2c and 2d sites but have finite structure factors otherwise.

It is possible that regions of local ordering could be linked to local changes in stoichiometry. This is expected in CZTS, where theoretical studies suggest that reduced Cu content (Cu-poor material) should reduce the density of Cu_{Zn} antisite defects and Cu-Zn disorder.[10] However, large area EDX mapping here showed no clear evidence for spatial variations in the Ag/Zn ratio.

3.2 Photoluminescence

Figure 7 shows PL spectra obtained for the slow-cooled and quenched samples. Figure 7a shows PL from the slow-cooled sample as a function of laser power, indicating a main peak at 1.345eV and a subsidiary peak at 1.27eV. The 1.345eV peak is relatively narrow and similar to the main emission lines recorded for AZTSe thin films (in the range 1.33-1.36eV), which have been interpreted as the band-edge emission.[11] The PL intensity from the quenched sample was an order of magnitude lower compared to the slow-cooled sample (Figure 7b), suggesting higher rates of non-radiative recombination. In addition, although the 1.345eV peak is clearly still present, the 1.27eV peak is either absent or has much reduced intensity relative to the dominant emission at 1.345 eV in the quenched sample.

Although attribution of the lower 1.27 eV peak is inconclusive, the most likely candidates appear to be either a SnSe secondary phase, which has a direct gap energy of 1.27eV,[24] or emission related to Ag-Zn disorder. Evidence of SnSe however, was not found in the XRD or TEM. The expected energies of other secondary phases are also not near the observed 1.27 eV peak (Ag_2Se = 0.15 eV, ZnSe = 2.7 eV, Ag_2SnSe_3 = 0.81 eV, $SnSe_2$ = 1.2 -3.0 eV).

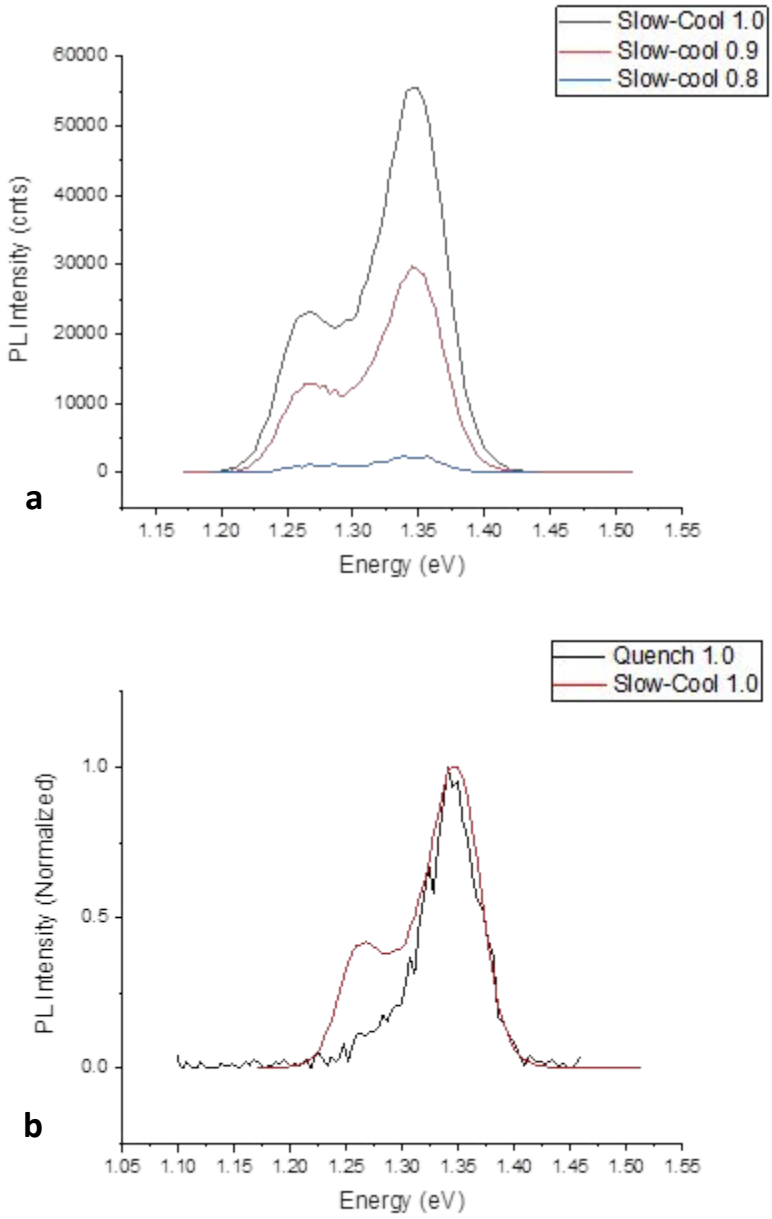

Figure 7: Room temperature PL (a) as a function of the laser power for the slow-cooled sample, (b) comparison of the quenched and slow-cooled samples at the same laser power

Considering intrinsic defects, a number of points in the literature suggest Ag-Zn related defect complex may be responsible. First, for all stable stoichiometries, the [Ag_{Zn}+Zn_{Ag}] defect complex is predicted to have the lowest formation energy.[25] Second, the shallow defect energy level measured by PL (0.07 eV from band edge) is the approximate energy predicted for

the Ag_{Zn} defect complex. Third, sample stoichiometry is expected to be near stoichiometric due to element weights during fabrication, which should limit formation of significant quantities of stoichiometry-altering substitutions (i.e. $V_{Ag} + Zn_{Ag}$). It is worth noting that the theoretical predictions[25] have been made for the sulphide system (Ag_2ZnSnS_4), and do not exist for the selenide, but significant deviations from the sulphide case are not expected, and are unlikely to change the points noted above.

It is interesting to note that the lower energy peak is less resolved in the quenched sample where more disorder is expected. This could be due to increased non-radiative recombination in the Ag-Zn anti-site domains for the quenched sample, or changes in the extent of bandgap fluctuations, which can be larger for slow-cooled samples due to the time allowed for domains to reach minimum energy state. Clearly further work is needed to investigate this point.

4. Conclusions

Although the rationale for Ag substitution of Cu in CZTSSe was to reduce antisite defect formation, the results here show that, in both the quenched and slow-cooled AZTSe, there is direct evidence for substantial Ag-Zn intermixing between the kesterite 2c (Ag) and 2d (Zn) sites and some Zn on the 2a (Ag) sites. Direct elemental mapping of the slow-cooled sample by EDX suggests that, over an area a few tens of nanometers across, there is complete intermixing of Ag and Zn on the 2c and 2d sites. However, individual HAADF images from both the quenched and slow-cooled samples show at least partial ordering of Ag and Zn between the 2c and 2d columns at the nanometer level, in agreement with XRD results. We have shown that these

results can be explained by a model where partially ordered twin-related domains exist in a more disordered matrix.

The results therefore imply that our AZTSe has high densities, albeit non-uniformly distributed, of Ag_{Zn} and Zn_{Ag} antisite defects, both at the growth temperature of 550°C, since the quenched sample should largely freeze in the high temperature structure, and despite slow-cooling which should maximise ordering. XRD suggests some evidence that slow-cooling increases the degree of Ag-Zn ordering on the 2c and 2d sites, although TEM suggests a similar domain structure is present in both the quenched and slow-cooled samples. The PL shows emission close to the expected bandgap, i.e. minimal band tailing, despite the Ag-Zn disorder, and that, for the slow-cooled sample, there is an emission peak at around 0.07eV below the expected band edge, which could be attributed to [Ag_{Zn} + Zn_{Ag}] antisite complex, although further evidence to assign a definitive attribution should be considered.

It is worth considering the implications of these results for understanding solar cells based on CZTSSe and Ag-substituted CZTSSe absorbers. Our results show that, even after a slow-cooling treatment, Ag substitution of Cu does not suppress extensive antisite defect formation, either in AZTSe, and, by implication, also not in less Ag-substituted ACZTSe alloys. Thus the progressive improvement in band tailing as the Ag content is increased is not due to a progressive reduction in the overall antisite defect density. As shown by Gerschon et al[12], Ag-substituted CZTSe films with Ag contents above about 50% substitution are not promising for use as solar cell absorbers owing to an extremely low carrier density, which should lead to poor junction formation. However, films with low Ag contents (5-10%) have much higher carrier densities and a significant improvement in ACZTSe solar cell efficiencies compared with CZTSe

cells has been demonstrated, consistent with the lower band tailing observed in the ACZTSe alloys.[12,26] The lower formation energies for Cu_{Zn} and Zn_{Cu} antisite defects suggest that there are also high densities of antisites in CZTSSe, as confirmed experimentally by a variety of techniques (see earlier). Neutron diffraction measurements also shows that slow-cooling of CZTSSe samples reduces but doesn't eliminate the total number of Cu-Zn antisite defects, although whether this reflects isotropic changes or the formation of ordered and disordered domains as in our case remains uncertain.[27] Given therefore that both CZTSSe and AZTSe contain substantial numbers of antisite defects, the generally greater band tailing observed in CZTSSe, up to 0.2-0.3eV below the band edge, needs explanation. In both CZTSSe and AZTSe, the Cu(Ag)-Zn antisite defect levels are similarly close to the band edge.[25] This implies that either there may be other active point defects present in CZTSSe that are not in AZTSe, or that longer range extrinsic microstructural features play a role and need to be considered in materials preparation treatments. Although the primary emphasis of the work here has been on Ag-Zn disorder, a preliminary analysis of microstructural defects showed that individual grains of AZTSe rarely contained either low- or high-angle grain boundaries, or dislocations. However, in previous work of CZTS, we have observed high densities of antisite domain boundaries, [13] and recent work by Mendis et al [28] have demonstrated similar results for CZTSe. Some of these antisite boundaries contain Sn antisite defects and can be charged. This should lead to local potential fluctuations and carrier trap states, both of which could contribute to band-tailing. The AZTSe samples here were found to contain antisite domain boundaries, but at densities less than 10^8 cm^{-2}, a factor of at least 10^2 times lower than we reported for CZTS.[13] Alternatively, theoretical studies have suggested that Cu and Zn clustering

is energetically favourable in CZTSSe, leading to local bandgap variations.[7,29] There is also strong experimental evidence for defect clustering in CZTSSe, for example from Raman and nuclear magnetic resonance (NMR) studies,[30] and from EELS studies, which suggest segregation into Cu-rich and Zn-rich regions over the 5-20nm range as noted earlier.[5,6] On the basis of their similar electronic structures, we would expect clustering to be favoured in both CZTSSe and AZTSe. However, we have found no evidence from EDX mapping for long range fluctuations in the Ag and Zn concentrations. It is possible that the size difference between the Ag^{+} and Zn^{2+} ions inhibits long-range Ag-Zn segregation in AZTSe compared to Cu-Zn segregation in CZTSSe. This could occur because Ag-rich and Zn-rich regions would be regions of compressional and dilatational strain respectively, leading to an increase in strain energy. However, more work is needed to clarify whether this is a significant energy contribution.

Acknowledgements

The authors are very grateful to R. Haight and T. Gershon, IBM Yorktown Heights, S. Lozano-Perez, Oxford University Department of Materials and D.J. Fermin, Bristol University School of Chemistry for insightful discussions and suggestions, and acknowledge EPSRC grants EP/K040375/1 and EP/L017792/1 for access to the JEOL ARM200CF (S)TEM (South of England Analytical Electron Microscope)

ASSOCIATED CONTENT Supporting Information Available: This shows more detail on the processing steps used in converting raw HAADF and EDX data into the final elemental maps in Figure 4

References

1. Wang W.; Winkler M.T.; Gunawan O.; Gokmen T.; Todorov T.K.; Zhu Y.; Mitzi D.B. Device Characteristics of CZTSSe Thin-film Solar Cells with 12.6% Efficiency *Adv. Energy Mater.* **2014**, *4*, 1301465
2. Schorr S. The Crystal Structure of Kesterite type Compounds: a Neutron and X-ray Study *Solar Energy Materials and Solar Cells* **2011**, *95*, 1482-1488
3. Bosson C.J.; Birch M.T.; Halliday D.P.; Knight K.S.; Gibbs A.S.; Hatton P.D. Cation Disorder and Phase Transitions in the Structurally Complex Solar Cell Material Cu_2ZnSnS_4 *J. Mater. Chem. A*, **2017**, *5*, 16672-16680
4. Valakh Y.; Kolomys O.F.; Ponomaryov S.S.; Yukhymchuk V.O.; Babichuk I.S.; Izquierdo-Roca V.; Saucedo E.; Perez-Rodriguez A.; Morante J.R.; Schorr S.; Bodnar I.V. Raman Scattering and Disorder Effect in Cu_2ZnSnS_4 *Phys. Stat. Sol. RRL*, **2013**, *7*, 258-261
5. Mendis B.G.; Shannon M.D.; Goodman M.C.J.; Major J.D.; Claridge R.; Halliday D.P.; Durose K. Direct Observation of Cu, Zn Cation Disorder in Cu_2ZnSnS_4 Solar Cell Absorber Material using Aberration corrected Scanning Transmission Electron Microscopy *Progress in Photovoltaics Research and Applications* **2014**, *22*, 24-34
6. Aguiar J.A.; Erkan M.E.; Pruzan D.S.; Nagaoka A.; Yoshino K.; Moutinho H.; Al-Jassim M.; Scarpulla M.A. Cation Ratio Fluctuations in Cu_2ZnSnS_4 at the 20nm Length Scale investigated by Analytical Electron Microscopy *Phys. Stat. Sol. (a)*, **2016**, *213*, 2392-2399
7. Scragg J.J.S.; Larsen J.K.; Kumar M.; Persson C.; Sendler J.; Siebentritt S.; Platzer-Bjorkman C. Cu-Zn Disorder and Bandgap Fluctuations in $Cu_2ZnSn(S,Se)_4$: Theoretical and Experimental Investigations *Phys. Stat. Sol. (b)*, **2016**, *253*, 247-254

8. Gokmen T.; Gunawan O.; Todorov T.K.; Mitzi D.B. Band Tailing and Efficiency Limitation in Kesterite Solar Cells *Appl. Phys. Lett*. **2013**, *103*, 103506

9. Liu X; Feng Y.; Cui H.; Liu F.; Hao X.; Conibeer G.; Mitzi D.B.; Green M. The Current Status and Future Prospects of Kesterite Solar Cells: a Brief Review *Prog. Photovoltaics*, **2016**, *24*, 879-898

10. Chen S.; Walsh A.; Gong X-G.; Wei S-H. Classification of Lattice Defects in Kesterite Cu_2ZnSnS_4 and $Cu_2ZnSnSe_4$ Earth-abundant Solar Cell Absorbers *Adv. Materials*, **2013**, *25*, 1522-1539

11. Chagarov E.; Sardashti K.; Kummel A.C.; Lee Y.S.; Haight R.; Gershon T.S. $Ag_2ZnSn(S,Se)_4$: A Highly Promising Absorber for Thin Film Photovoltaics *J. Chem. Phys.* **2016,** *144*, 104704

12. Gershon T.S.; Lee Y.S.; Antunez P.; Mankad R.; Singh S.; Bishop D.M.; Gunawan O.; Hopstaken M.; Haight R. Photovoltaic Materials and Devices based on the Alloyed Kesterite Absorber $(Ag_xCu_{1-x})_2ZnSnSe_4$ *Adv. Energy Mater.* **2016**, *6*, 1502468

13. Kattan N.A.; Griffiths I.J.; Cherns D.; Fermin D.J. Observation of Antisite Domain Boundaries in Cu_2ZnSnS_4 by Atomic Resolution Transmission Electron Microscopy *Nanoscale*, **2016**, *8*, 14369-14373

14. Bishop D.M.; McCandless B.E.; Haight R.; Mitzi D.M.; Birkmire R.W. Fabrication and Electronic Properties of CZTSe Single Crystals *IEEE J. Photovoltaics*, **2015**, *5*, 390-394

15. Gong W.; Tabata T.; Takei K.; Morihama M.; Maeda T.; Wada T. Crystallographic and Optical Properties of $(Cu,Ag)_2ZnSnS_4$ and $(Cu,Ag)_2ZnSnSe_4$ Solid Solutions *Phys. Status Solidi C* **2015** *12*, 700-703

16. L. Jones, A. Varambhia, R. Beanland, D. Kepaptsoglou, I. Griffiths, A. Ishizuka, F. Azough, R. Freer, K. Ishizuka, D. Cherns, Q. Ramasse, S. Lozano-Perez, P.D. Nellist, Managing Dose-, Damage- and Data-rates in Multi-frame Spectrum-imaging *Microscopy* **2018**, *67, Issue Suppl_1*, i98-i113

17. Jones L.; Yang H.; Pennycook T.J.; Marshall M.S.J.; Van Aert S.; Browning N.D.; Castell M.; Nellist P.D. Smart Align - A New Tool for Robust Non-rigid Registration of Scanning Microscope Data *Adv. Structural and Chemical Imaging* **2015,** *1*, 8

18. Egerton R.F. Electron Energy Loss Spectroscopy in the Electron Microscope, Springer **2011**

19. S. Chen S.; Walsh A.; Luo Y.; Yang J-H.; Gong X.G.; Wei S-H. Wurtzite-derived Polytypes of Kesterite and Stannite Quaternary Chalcogenide Semiconductors *Phys. Rev. B* **2010**, *82*, 195203

20. Chu M-W.; Liou S.C.; Chang C-P.; Choa F-S.; Chen C.H. Emergent Chemical Mapping at Atomic-column Resolution by Energy Dispersive X-ray Spectroscopy in an Aberration-corrected Electron Microscope *Phys. Rev. Lett*. **2010**, *104*, 196101

21. Rosenauer A.; Mehrtens T.; Müller K.; Gries K.; Schowalter M.; Satyam P.Y.; Bley S.; Tessarek C.; Hommel D.; Sebald K.; Seyfried M.; Gutowski J.; Avramescu A.; Engl K.; Lutgen S. Composition Mapping in InGaN by Scanning Transmission Electron Microscopy *Ultramicroscopy* **2011,** *111*, 1316-1327

22. T. Walther, A New Experimental Procedure to Quantify Annular Dark Field Images in Scanning Transmission Electron Microscopy *J. Microsc.*, **2006**, *221*, 137-144

23. Wang Z.W. Li Z.Y.; Park S.J.; Abdela A.; Tang D.; Palmer R.E. Quantitative Z-contrast Imaging in the Scanning Transmission Electron Microscope with Size-selected Clusters *Phys. Rev. B*, **2011**, *84*, 073408

24. Soliman H.S; Abdel Hady D.A.; Abdel Rahman K.F.; Youssef S.B.; El-Shazly A.A. Optical Properties of tin Selenid Films *Physica A: Statistical mechanics and its applications* **1995**, *216*, 77-84

25. Yuan Z-K.; Chen S. Xiang H.; Gong X-G.; Walsh A.; Park J-S.; Repins I.; Wei S-H. Engineering Solar Cell Absorbers by Exploring the Band Alignment and Defect Disparity: The Case of Cu- and Ag-based Kesterite Compounds Adv. Functional Materials **2015**, *25*, 6733-6743

26. Hages C.J; Koeper M.J; Agrawal R. Optoelectronic and Material Properties of Nanocrystal-based CZTSe Absorbers with Ag Alloying, *Solar Energy Materials and Solar Cells* **2016**, *145*, 342-348

27. Mendis B.G.; McKenna K.P.; Gurieva G.; Rumsey M.F.; Schorr S. Crystal Structure and Antisite Boundary Formation in $Cu_2ZnSnSe_4$ *J. Mater. Chem*. **2018**, *6*, 189-197

28. Bishop D.M.; McCandless B.; Gershon T.S.; Lloyd M.A.; R. Haight R.; Birkmire R. Modification of Defects and Potential Fluctuations in Slow-cooled and Quenched $Cu_2ZnSnSe_4$ Single Crystals *J. Appl. Phys.*, **2017**, *121*, 065704

29. Huang D.; Persson C. Band Gap Change induced by Defect Complexes in Cu_2ZnSnS_4 *Thin Solid Films*, **2013**, *535*, 265-269

30. Paris M.; Choubrac L.; Lafond A.; Guillot-Deudon C.; Jobic S. Solid-state NMR and Raman Spectroscopy to address the Local Structure of Defects and the Tricky Issue of the Cu/Zn disorder in Cu-poor, Zn-rich CZTS materials *Inorg. Chem.*, **2014**, *53*, 8646-8653

Table of Contents graphic